An XFEM-based numerical model to calculate conductivity of propped fracture considering proppant transport, embedment and crushing

Fang Shi[a,b], XiaoLong Wang[a], Chuang Liu[a], He Liu[c], HengAn Wu[a,*]

[a] CAS Key Laboratory of Mechanical Behavior and Design of Materials, Department of Modern Mechanics, University of Science and Technology of China, Hefei, 230027, Anhui, China
[b] Jiangsu Key Laboratory of Advanced Manufacturing Technology, Huaiyin institute of technology, Huai'an, 223003, Jiangsu, China
[c] PetroChina Research Institute of Petroleum Exploration & Development, 20 Xueyuan Road, Haidian District, 100083, Beijing, China

ARTICLE INFO

ABSTRACT

The accurate conductivity evaluation of propped hydraulic fracture is crucial for the design and optimization of hydraulic fracturing treatments to achieve economic production of hydrocarbon. In this paper, a coupled numerical model in consideration of transport, placement, deformation, embedment and crushing of proppant is proposed to calculate the conductivity within the framework of the extended finite element method (XFEM). In the model, the fluid-solid coupling equations are simultaneously solved. The proppant transport is modeled using the upwind method. The Hertz contact model is used to obtain the width of propped fracture considering the deformation and embedment of proppant. A damage model is proposed to describe the conductivity reduction of the proppant pack due to grain failure. Size effects on the strength of proppant are considered using Weibull distribution and Griffith theory. After comparison with experimental data, the proposed model is employed to conduct sensitivity studies of several parameters on fracture conductivity. Results show that the most sensitive factor is proppant size, followed by proppant concentration, pumping rate of slurry, elastic modulus of proppant, and pumping strategy of proppant. The effects of elastic modulus of formation and Poisson's ratios of proppant and formation are negligible in comparison to other factors. It is also found that with the increase of proppant size, the fracture conductivity increases initially and decreases after reaching a peak. This paper contributes to a better understanding of the effects of related factors on fracture conductivity and provides a useful numerical tool for proppant selection in hydraulic fracturing design.

1. Introduction

Hydraulic fracturing is a widely used well stimulation technology in the oil and gas industry. The objective of hydraulic fracturing is to generate and maintain the conductive flow path between the wellbore and the formation. To this end, the high-pressure fluid is pumped to overcome the breakdown pressure of the formation to create hydraulic fractures. During the process, proppants such as sand or ceramic are injected with the fluid into fractures to keep fractures open after the fluid pressure is released. Field evidence, laboratory experiments and numerical studies show that the proppant selection (type, size, amount etc.) plays critical roles in improving fracture network conductivity and achieving economic production rates (Economides and Martin, 2007; Tomac and Gutierrez, 2013; Tong and Mohanty, 2016; Yu et al., 2015). Thus, it is of great significance to investigate the impacts of proppant and related factors on fracture conductivity.

During the past decades, a lot of experimental and theoretical

studies on the conductivity of propped fracture have been carried out, indicating that the conductivity is relevant to many variations such as closure stress, proppant size, proppant mechanical properties, proppant concentration and distribution, proppant deformation, proppant crushing, proppant embedment, formation mechanical properties, and so on. For instance, Cooke (1975) described a theoretical model to evaluate the effects of fracturing fluids on fracture conductivity and compared model predictions with laboratory experimental results. He (Cooke, 1975) found that the factors that play important roles in conductivity reduction include concentration of proppant, amount of residue in the fluid, and porosity of the proppant. Lacy et al. (1997, 1998) experimentally studied the effects of fluid viscosity, proppant size, closure stress, and leak-off rate on proppant embedment. They (Lacy et al., 1997, 1998) found that closure stress is the primary factor that determines embedment, with proppant size and proppant concentration also being important. Fredd et al. (2001) studied the effects of proppant concentration, proppant strength, and formation properties on fracture

---

conductivity through a series of laboratory conductivity experiments, and found that conductivity can be proppant- or asperity-dominated, depending on the proppant concentration, proppant strength, and formation properties. Awoleke et al. (2012) carried out a systematic investigation and found that the effects arranged in order of decreasing effect on conductivity are closure stress, temperature, and proppant concentration. Rivers et al. (2012) performed a series of laboratory experiments and studied the effects of proppant concentration and closure stress, and it is observed that increasing proppant concentration in the fracture shows higher conductivity values in some cases, while increasing the closure stress results in a significant loss in conductivity for all cases. Alramahi and Sundberg (2012) studied the effect of proppant embedment in shales on hydraulic fracture conductivity and proposed an analytical model to calculate the conductivity of hydraulic fractures based on their laboratory measurements. They (Alramahi and Sundberg, 2012) found that the same physical mechanisms responsible for proppant embedment are also responsible for the loss of fracture conductivity. Neto et al. (2015) developed a mathematical model which incorporates the effects of proppant compressibility and in-situ stresses to evaluate the performance of the hydraulic fracture partially filled with proppant pack. Gao and Li et al. (Gao et al., 2012; Li et al., 2015) derived an analytical model to calculate the width of propped fracture in consideration of proppant deformation and embedment, and their calculation models adequately matched experimental results. Shekhawat and Pathak (2016) developed a new equipment for onsite testing and proposed a new method to determine permeability reduction of monolayer proppant pack with increasing closure pressure. Li et al. (2016) also created a new mathematical model, which considers factors including the particle size, closure pressure, strains of the rock and proppants, embedment, crushing rate, looseness coefficient and so on, to calculate proppant-packed fracture conductivity. In addition to those mentioned above, some other factors affecting fracture conductivity such as conductivity damage due to fracturing fluid (Zhang et al., 2015), non-Darcy flow effect (Lopez-Hernandez et al., 2004) have also been studied.

From the point of view of engineering design, it is difficult to optimally select proppant just based on experience or theoretical knowledge. The reason is that the proppant-related problems are quite complicated as they involve various proppant-related physical processes including proppant migration along fractures, gravitational settlement of proppant, deformation of proppant, embedment of proppant particles into the surface of hydraulic fracture, and proppant crushing. Consequently, some numerical models have been proposed by researchers to gain a better understanding of proppant-related problems. For instance, Ouyang et al. (1997) proposed a numerical model together with an adaptive finite element procedure to study the proppant distribution in a propagating hydraulic fracture. In his study (Ouyang et al., 1997), however, there are several subtle issues that arise regarding the coupling between the gridding problem and the fluid-fracture calculation. Weng et al. (2011) developed a hydraulic fracture model based on the displacement discontinuity method (Crouch and Starfield, 1983) to simulate complex fracture network propagation in consideration of proppant transport. In their study (Weng et al., 2011), the width of each fracture is calculated according to an analytical solution. In order to investigate an unsuccessful hydraulic fracturing operation in the North Germany Basin, Zhou et al. (2014) developed a numerical model to simulate fracture propagation, closure, contact, and proppant transport based on the finite volume method and the finite difference method. They (Zhou et al., 2014) found that although the lower part of the fracture was propped, the middle part was fully closed without any support from the proppant if the perforation has not been set 15 m lower. Dontsov and Peirce (2015) developed a numerical model capable of capturing both tip screen-out and gravitational settling effects and found that the particles can reach the tip of the fracture even without leak-off. Kong et al. (2015) developed a coupled numerical model considering proppant transport and investigated the effects

of several factors on hydraulic fracturing performance, and found that reservoir matrix permeability, proppant volume and relative proppant/fluid density have the highest impact on hydraulic fracturing efficiency. Raymond et al. (2015) modeled the proppant distribution in a formation containing natural fractures using the material point method (Sulsky et al., 1994), and simulation results show that fractures oriented in directions close to the hydraulic fracture direction facilitate the proppant placement. Han et al. (2016a) proposed a coupled geomechanics and fluid flow model considering the failure of proppant pack and fracture conductivity damage, and found that proppant near the wellbore has a higher likelihood of being crushed. Han et al. (2016b) proposed a new computational fluid dynamic models to simulate the proppant transport within complex fracture geometries, and found that at fracture junctions, turbulent flow regime will develop and help proppant transport to natural fractures. Shiozawa and McClure (2016) performed simulations of proppant transport in an Eulerian–Eulerian framework considering proppant settling due to gravity, tip screen-out, and fracture closure, and they concluded that proppant tends to accumulate at the intersections between natural and hydraulic fractures.

The extended finite element method (XFEM) (Belytschko and Black, 1999; Moës et al., 1999) has been proved to be an efficient tool for the numerical modeling of fracture propagation. In the XFEM, no remeshing is required during fracture propagation, and the discontinuities can be modeled by introducing additional enriched degrees of freedom (DOFs) to the nodes whose support domains are cut by fractures (Belytschko and Black, 1999; Moës et al., 1999). In recent years, attracted by the great advantages of XFEM, some researchers have utilized it to investigate hydraulic fracturing problems such as basic coupling algorithms (Gordeliy and Peirce, 2013a, 2013b; Lecampion, 2009), hydraulic fracture propagation in porous media (Mohammadnejad and Khoei, 2013a, 2013b), and interaction between the hydro-fracture and the frictional natural fracture (Dahi-Taleghani and Olson, 2011; Khoei et al., 2015, 2016; Shi et al., 2017; Taleghani and Olson, 2014). In our recent work (Shi et al., 2016), we established a fully coupled XFEM-based approach for modeling hydraulic fracturing in consideration of the transport and placement of proppant. In that model, the proppant is treated as a rigid body, and the propped fracture is modeled by applying displacement boundary conditions to restrict the normal closure of propped fracture. In reality, the width of propped fracture will decrease due to the deformation, embedment and crushing of proppant under the increasing closure stress after the pumping is completed (Han et al., 2016a). Additionally, the width of propped fracture is the major factor that influences the fracture conductivity (Alramahi and Sundberg, 2012). Thus, it is of great importance to take the proppant deformation, embedment and crushing into account when calculating fracture conductivity. To this aim, a more sophisticated numerical model is developed in this study.

As stated above, numerous studies on fracture conductivity have been conducted. It still lacks, however, an effective numerical model to perform studies on the complicated process of hydraulic fracturing in comprehensive consideration of proppant, and facilitate hydraulic fracturing design, such as proppant selection based on collected field data and the other design parameters. As a result, in this paper, we will present a fully-coupled numerical model to simulate the hydraulic fracturing process and calculate the conductivity of the propped fracture in the context of XFEM. Several key physical processes including proppant transport, placement, deformation, embedment, and crushing, as well as the size effect of proppant grains on strength (Tsoungui et al., 1999) are considered to gain a complete picture of how various variables influence the fracture conductivity. Finally, on the basis of the proposed model, we will conduct a sensitivity analysis of several factors on fracture conductivity, including proppant size, elastic moduli of proppant and formation, Poisson's ratios of proppant and formation, pumping rate of slurry, proppant concentration and pumping strategy of proppant.
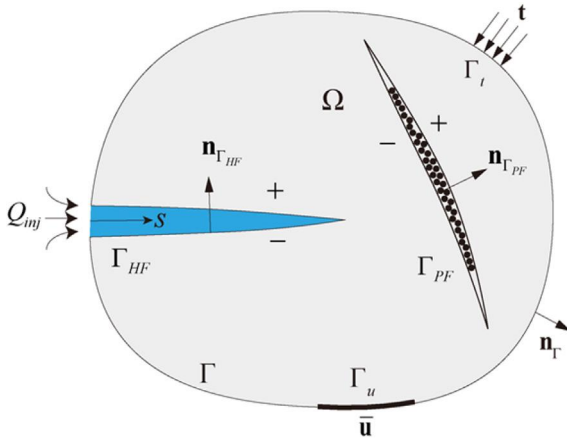
Fig. 1. Illustration of a domain containing a hydro-fracture filled with high-pressure fluid and a propped fracture.

2. Problem formulation and solution approaches

Consider a two-dimensional domain Ω containing a hydraulically driven fracture Γ_{HF} filled with high-pressure incompressible fluid, as depicted in Fig. 1. The domain also contains a propped fracture Γ_{PF} filled with proppant. The boundary of the domain is Γ and the unit outward normal vector of Γ is represented by $\mathbf{n}_\Gamma$. The prescribed tractions $\mathbf{t}$ and the displacements $\overline{\mathbf{u}}$ are imposed on the boundary Γ_t and Γ_u, respectively. The two faces of fractures are expressed by the positive "+" and the negative "−" signs. The unit outward normal vectors of negative faces of the hydro-fracture Γ_{HF} and the propped fracture Γ_{PF} are donated by $\mathbf{n}_{\Gamma_{HF}}$ and $\mathbf{n}_{\Gamma_{PF}}$, respectively. The slurry is injected at a constant rate of Q_{inj}. In order to describe the flow of slurry, a one-dimensional curvilinear coordinate system (donated by s) is defined along the hydro-fracture, and the origin of the coordinate system is positioned at the pumping point.

Some assumptions are made in this study. Generally, the slurry behaves as a non-Newtonian fluid. However, it can be assumed as a Newtonian fluid for simplicity in computer simulation of hydraulic fracturing (Adachi et al., 2007; Hammond, 1995; Tomac and Gutierrez, 2013). We assume that the propagation of the fracture is a quasi-static process, and no fluid lag exists between the fracture tip and the fluid front. The formation is considered as a brittle material and an impermeable media. The gravitational settling of proppant, which might not be particularly significant for the relatively lightweight proppant or the relatively high viscosity slurry (Zoveidavianpoor and Gharibi, 2015), is not taken into account. In addition, the proppant flow back, grain migration and gel damage are also not taken into consideration in this paper.

2.1. Deformation of formation

The strong form of the equilibrium equation of the domain in the absence of body forces can be expressed as

$$\nabla \cdot \boldsymbol{\sigma} = \mathbf{0} \quad \text{in } \Omega \tag{1}$$

where $\boldsymbol{\sigma}$ is the Cauchy stress tensor, and $(\nabla \cdot)$ is the divergence operator. The boundary conditions can be written as

$$\begin{cases} \mathbf{u} = \overline{\mathbf{u}} & \text{on } \Gamma_u \\ \boldsymbol{\sigma} \cdot \mathbf{n} = \mathbf{t} & \text{on } \Gamma_t \\ \boldsymbol{\sigma} \cdot \mathbf{n}_{\Gamma_{HF}} = p\mathbf{n}_{\Gamma_{HF}} & \text{on } \Gamma_{HF} \\ \boldsymbol{\sigma} \cdot \mathbf{n}_{\Gamma_{PF}} = \mathbf{t}^{propped} & \text{on } \Gamma_{PF} \end{cases} \tag{2}$$

where p represents the fluid pressure, $\mathbf{t}^{propped}$ is the traction vector acting on the faces of propped fracture Γ_{PF}.

Linear elastic constitutive is applied to describe the behavior of the formation, that is

$$\boldsymbol{\sigma} = \mathbf{D} : \boldsymbol{\varepsilon} \tag{3}$$

in which $\mathbf{D}$ is the elasticity matrix, $\boldsymbol{\varepsilon}$ is the strain tensor associated with displacement $\mathbf{u}$. Under the assumption of small deformation, $\boldsymbol{\varepsilon}$ can be determined from

$$\boldsymbol{\varepsilon} = \frac{1}{2}(\nabla \mathbf{u} + (\nabla \mathbf{u})^T) \tag{4}$$

2.2. Flow of slurry and proppant

The one-dimensional flow of slurry and proppant in the hydro-fracture must satisfy the mass conservation equation. As the fluid is assumed to be incompressible with Newtonian rheology and there is no fluid leak-off, the continuity equations can be expressed as follows for any point s along the hydro-fracture

$$\frac{\partial w}{\partial t} + \frac{\partial q_s}{\partial s} - Q_{inj}\delta(s) = 0 \tag{5}$$

$$\frac{\partial(cw)}{\partial t} + \frac{\partial(cq_s)}{\partial s} - c_{inj}(t)Q_{inj}\delta(s) = 0 \tag{6}$$

where w represents the width of the hydro-fracture; c is the proppant volumetric concentration of the slurry defined as the fraction of the volume occupied by the proppant; q_s is the slurry flux; $\delta(*)$ is the Dirac delta function, and $c_{inj}(t)$ represents the volumetric concentration of proppant pumped at the pumping point at time instant t. It should be noted that the proppant would be prevented from passing through the narrow portion, for example, the near-tip region, if the proppant size is larger than the width of the fracture. It is assumed that the flow in the fracture is laminar flow and has a low Reynolds number (Adachi et al., 2007). Therefore, the fluid flow inside the fracture can be simplified to the flow along a channel by using lubrication theory (Adachi et al., 2007). Under the framework of the lubrication theory, the slurry flux within the hydro-fracture can be given by the Poiseuille's law (Batchelor, 1967)

$$q_s = -\frac{w^3}{12\mu(0)}f_s\frac{\partial p}{\partial s} \tag{7}$$

where $\mu(0)$ is the viscosity of the slurry without proppant. f_s is a non-dimensional function defined as

$$f_s = \frac{2\mu(0)}{3\mu(c)} \tag{8}$$

where $\mu(c)$ is the effective viscosity of the slurry given as (Zhou et al., 2014)

$$\mu(c) = \mu(0)\left(1 - \frac{c}{\hat{c}}\right)^{-m} \tag{9}$$

In the above equation, the exponent m and the saturation concentration $\hat{c}$ are taken as 1.05 (Adachi et al., 2007) and 0.6, respectively, in this paper. Substituting Eq. (7) into Eq. (5) leads to the following Reynolds equation

$$\frac{\partial w}{\partial t} - \frac{\partial}{\partial s}\left(k\frac{\partial p}{\partial s}\right) - Q_{inj}\delta(s) = 0 \tag{10}$$

where $k = \frac{w^3}{12\mu(0)}f_s$. Eq. (10) can be solved with the following initial and boundary conditions

$$\begin{cases} w(s, 0) = 0 \\ w(s_{tip}, t) = 0 \\ q_s(0, t) = Q_{inj} \\ q_s(s_{tip}, t) = 0 \end{cases} \tag{11}$$

and the global mass conservation equation

$$\int_0^{s_{tip}} w ds = \int_0^t Q_{inj} dt \tag{12}$$

In the above, s_{tip} represents the location of the hydro-fracture tip.

2.3. Weak form of governing equations

By introducing the trial function $\mathbf{u}\,(\mathbf{x}, t)$ and test function $\delta\mathbf{u}\,(\mathbf{x}, t)$ for the displacement field, the weak form of equilibrium equation can be expressed as

$$\int_\Omega \delta\varepsilon\!: \sigma d\Omega + \int_{\Gamma_{HF}} \langle\delta\mathbf{u}\rangle\cdot p\mathbf{n}_{\Gamma_{HF}} d\Gamma + \int_{\Gamma_{PF}} \langle\delta\mathbf{u}\rangle\cdot \mathbf{t}^{propped} d\Gamma = \int_{\Gamma_t} \delta\mathbf{u}\cdot\mathbf{t}d\Gamma \tag{13}$$

where the symbol $\langle*\rangle = *^+ - *^-$ represents the difference of the variable "$*$" between face "$+$" and face "$-$" of fractures. Therefore, $\langle\mathbf{u}\rangle$ stands for the displacement jump across the faces of fractures.

By introducing test function $\delta p\,(s, t)$, the weak form of the Reynolds equation (Eq. (10)) can be given as

$$\int_{\Gamma_{HF}} \left(\delta p \frac{\partial w}{\partial t} + \frac{\partial(\delta p)}{\partial s}k\frac{\partial p}{\partial s} \right)d\Gamma + \delta p\Big|_{s=0} Q_{inj} = 0 \tag{14}$$

2.4. Discretization of governing equations

To discrete the equilibrium equation, the XFEM is employed to approximate the displacement field $\mathbf{u}$. For the hydraulic fracturing problem, the displacement $\mathbf{u}$ for any point $\mathbf{x}$ in the domain Ω can be approximated by adding two types of enrichment shape functions as

$$\mathbf{u}(\mathbf{x}) = \sum_{I\in N_{all}} N_I^u(\mathbf{x})\mathbf{u}_I + \sum_{I\in N_{frac}} N_I^u(\mathbf{x})H(\mathbf{x})\mathbf{a}_I + \sum_{I\in N_{tip}} N_I^u(\mathbf{x}) \sum_{l=1}^4 F_l(\mathbf{x})\mathbf{b}_I^l \tag{15}$$

where N_{all} is the set of all nodes in the mesh, N_{frac} is the set of nodes whose support domains are cut into two parts by the fracture, and N_{tip} is the set of nodes whose support domains are partially cut by the fracture. N_I^u is the standard finite element shape functions of node I. $\mathbf{u}_I$ is the standard nodal displacement vector. $\mathbf{a}_I, \mathbf{b}_I^l$ ($l = 1,4$) are the nodal enriched DOF vectors. $H(\mathbf{x})$ and $F_l(\mathbf{x})$ are the enrichment shape functions to account for the displacement jump across fracture surfaces and the singular displacement field around the fracture tip, respectively. $H(\mathbf{x})$ is usually taken as the signed Heaviside function; $F_l(\mathbf{x})$ for the tip enrichment in brittle materials takes the general form:

$$\{F_l(r, \theta)\}_{l=1}^4 = \left\{ \sqrt{r}\sin\frac{\theta}{2},\ \sqrt{r}\cos\frac{\theta}{2},\ \sqrt{r}\sin\theta\sin\frac{\theta}{2},\ \sqrt{r}\sin\theta\cos\frac{\theta}{2} \right\} \tag{16}$$

where (r, θ) defines the polar coordinate system with the origin at the fracture tip.

To approximate the one-dimensional pressure field $p\,(s, t)$ inside a hydro-fracture, the fracture interface Γ_{HF} is discretized into fluid elements using linear shape functions. The nodes of the fluid elements are regularly arranged at the intersections of hydro-fractures and edges of solid elements, as well as the fracture tips. Thus, the finite element approximation of the pressure field can be expressed as

$$p(s) = \sum_{I\in N_{hf}} N_I^p(s)p_I \tag{17}$$

where N_{hf} is the set of nodes of the fluid elements defined along the hydraulic fracture; $N_I^p(s)$ represents the linear shape function of nodal pressure p_I for fluid node I, and it is defined in the natural local coordinate system ξ, namely

$$\begin{cases} N_1^p(\xi) = (\xi - 1)/2 \\ N_2^p(\xi) = (\xi + 1)/2 \end{cases} \tag{18}$$

The fracture opening displacement vector $\mathbf{w}$ can be approximated

by

$$\mathbf{w} = \sum_{I\in N_w} N_I^w\mathbf{u}_I \equiv \mathbf{N}^w\mathbf{U} \tag{19}$$

where N_w represents the set of nodes of elements that contain the fluid nodes; $\mathbf{N}^w$ is the shape function matrix which transfers the nodal displacement to fracture opening; $\mathbf{U}$ is the global nodal displacement vector.

By substituting the displacement and pressure approximations (Eq. (15), (17) and (19)) and the linear elastic constitutive equation (Eq. (3)) into the weak form of the equilibrium equation (Eq. (13)) and the slurry flow equation (Eq. (14)), it is straightforward to obtain the discretized system of the nonlinear coupled equilibrium and flow continuity equations as

$$\mathbf{KU} - \mathbf{QP} - \mathbf{F}^{ext} = \mathbf{0} \tag{20}$$

$$\mathbf{Q}^T\dot{\mathbf{U}} + \mathbf{HP} + \mathbf{S} = 0 \tag{21}$$

In Eq. (20), $\mathbf{K}$ is the global stiffness matrix:

$$\mathbf{K} = \begin{bmatrix} \int_\Omega (\mathbf{B}^{std})^T\mathbf{DB}^{std}d\Omega & \int_\Omega (\mathbf{B}^{std})^T\mathbf{DB}^{enr}d\Omega \\ \int_\Omega (\mathbf{B}^{enr})^T\mathbf{DB}^{std}d\Omega & \int_\Omega (\mathbf{B}^{enr})^T\mathbf{DB}^{enr}d\Omega + \int_{\Gamma_{PF}} (\mathbf{N}^w)^T\mathbf{D}^{propped}\mathbf{N}^wd\Gamma \end{bmatrix} \tag{22}$$

where $\mathbf{B}$ is the matrix of shape function derivatives; the matrix $\mathbf{D}^{propped}$ represents the constitutive relation between $\mathbf{t}^{propped}$ and fracture width $\mathbf{w}$, namely, $d\mathbf{t}^{propped} = \mathbf{D}^{propped}d\mathbf{w}$. The detail of $\mathbf{D}^{propped}$ will be given in Section 2.7. The coupling matrix $\mathbf{Q}$ that transfers fluid pressure vector $\mathbf{P}$ into equivalent nodal forces and the external loading vector $\mathbf{F}^{ext}$ are defined as

$$\mathbf{Q} = \int_\Omega (\mathbf{N}^w)^T\mathbf{n}_{\Gamma_{HF}}\mathbf{N}^p d\Omega \tag{23}$$

$$\mathbf{F}^{ext} = \int_{\Gamma_t} (\mathbf{N}^u)^T\mathbf{t}d\Gamma \tag{24}$$

In Eq. (21), the flow matrix $\mathbf{H}$ and the source term $\mathbf{S}$ are defined as

$$\mathbf{H} = \int_{\Gamma_{HF}} k\left(\frac{\partial\mathbf{N}^p}{\partial s}\right)^T\frac{\partial\mathbf{N}^p}{\partial s}ds \tag{25}$$

$$\mathbf{S} = \mathbf{N}^p(s)^T\big|_{s=0} Q_{inj} \tag{26}$$

Taking time integration of Eq. (21) over a time step, we can obtain

$$\int_{t_n}^{t_{n+1}} (\mathbf{Q}^T\dot{\mathbf{U}} + \mathbf{HP} + \mathbf{S})dt = \mathbf{0} \tag{27}$$

where n represents the time step number. Implicit backward Euler time discretization is employed in this paper, so according to Eq. (27), we have

$$\mathbf{Q}^T(\mathbf{U}_{n+1} - \mathbf{U}_n) + \Delta t\mathbf{HP}_{n+1} + \Delta t\mathbf{S} = \mathbf{0} \tag{28}$$

where $\mathbf{U}_{n+1}$, $\mathbf{P}_{n+1}$ are the unknown displacement field and fluid pressure at the $(n + 1)$th time step, respectively; $\mathbf{U}_n$ is the already known displacement field at the previous time step; Δt is the time increment between two adjacent time steps. In addition, after the time discretization, Eq. (20) can be rewritten as follows in every time step

$$\mathbf{K}_n\mathbf{U}_{n+1} - \mathbf{QP}_{n+1} - \mathbf{F}^{ext} = \mathbf{0} \tag{29}$$

Finally, $\mathbf{U}_{n+1}$, $\mathbf{P}_{n+1}$ can be obtained by solving the coupled Eqs. (28) and (29).

2.5. Coupling approach

Within each time step, the equilibrium equation (Eq. (29)), the slurry flow equation (Eq. (28)) and the proppant transport equation (Eq. (6)) must all be solved. Firstly, this nonlinear coupled system (Eq. (29) and (28)) is solved simultaneously using the Newton-Raphson

iterative method. Secondly, the proppant transport equation (Eq. (6)) is solved at the end of each time step as follows. The proppant concentration obtained from the last time step (donated by c_{last}) is applied to calculate the effective viscosity $\mu(c_{last})$ according to Eq. (9). After some manipulations, Eq. (6) can be rewritten as

$$\frac{\partial c}{\partial t} + \chi \frac{\partial c}{\partial s} = 0 \tag{30}$$

in which $\chi = -\frac{w^2}{24\mu(c_{last})}\frac{\partial p}{\partial s}$. Thus, this linear convection equation can be solved by the upwind difference scheme (Hirsch, 1990), that is

$$c_i^{\tilde{n}+1} = c_i^{\tilde{n}} - \Delta\tilde{t}(\chi^+ c_s^- + \chi^- c_s^+) \tag{31}$$

Where $\tilde{n}$ and $\Delta\tilde{t}$ represent step number and step size of the upwind scheme, respectively, and $\chi^+ = \max(\chi, 0)$, $\chi^- = \min(\chi, 0)$, $c_s^+ = (c_{i+1}^n - c_i^n)/\Delta s$, $c_s^- = (c_i^n - c_{i-1}^n)/\Delta s$. The above scheme is stable if $|\chi\frac{\Delta\tilde{t}}{\Delta s}| \leq 1$ can be satisfied. In this study, a second-order correction with a limiter is applied to reduce the numerical diffusion and dispersion (Adachi et al., 2007; Hirsch, 1990).

2.6. Width and conductivity of propped fracture considering proppant deformation, embedment and crushing

The statuses of proppant inside a fracture at different phases of fracturing are schematically illustrated in Fig. 2. In reality, the proppant has widely varying diameters. For example, a proppant sized to 30/50 mesh has proppant grains sized from 595 to 297 microns in diameter. However, it is quite difficult to establish mathematical models considering proppant with varying diameters. Hence, in this study, it is assumed that the proppant grains have the same diameter D_p. In addition, after the hydraulic pressure is released, proppant grains are assumed to be arranged in the hexagonal close packing, as shown in Fig. 2b. When the closure stress is equal to zero, the width of propped fracture $w_p^o(s)$ for any point s along the propped fracture can be determined by $w_p^o(s) = w_o(s)c(s)/\eta$, where $w_o(s)$ is the fracture width at point s before the fracture starts to close, as shown in Fig. 2a, and η represents the packing density (Steinhaus, 1999) and equals 0.74 for the hexagonal close packing pattern.

Afterwards, the fracture width will decrease from w_p^o to w_p due to the deformation and embedment of proppant in the presence of in-situ stress acting on the faces of propped fracture. Recently, an analytical model based on the Hertzian contact theory (Johnson, 1985) to calculate w_p by considering proppant deformation and embedment has been derived by Li et al. (2016). In this model, the spacing between the particles is assumed to be a small value and the contact of particles in the transverse fracture direction has not been considered. The deformation of half-space under proppant grain i due to the force on proppant grain i has been considered. However, the deformation of half-space under proppant grain i due to the force on proppant grain j has not been considered, i.e., the mechanical interaction (Hopkins, 2000; Kamali and Pournik, 2016) has not been taken into account. It

should be noted that this simplification may result in overestimation of the normal stiffness of the propped fracture (Hopkins, 2000; Kamali and Pournik, 2016). According to this model, w_p can be calculated by:

$$w_p = w_p^o - 1.89D_p p_{closure}^{2/3}[(n_1 - 1)T_1^{2/3} + T_2^{2/3}] \tag{32}$$

where

$$\begin{cases} n_1 = ceil\left(0.986\frac{w_p^o}{D_p}\right) \\ T_1 = \frac{1 - \nu_p^2}{E_p} \\ T_2 = \frac{1 - \nu_p^2}{E_p} + \frac{1 - \nu^2}{E} \end{cases} \tag{33}$$

In the above equations, n_1 is the number of proppant layers and *ceil* (x) is a ceiling function ($ceil(x) = |x| + 1$); $p_{closure}$ is the closure stress (or closure pressure); E_p and ν_p are elastic modulus and Poisson's ratio of the proppant, respectively; E and ν are elastic modulus and Poisson's ratio of the formation, respectively.

Li et al. (2016) also derived the permeability of the propped fracture according to the Carman-Kozeny equation, i.e., $k = \frac{\phi r^2}{8\tau^2}$, where ϕ, τ, and r represent fracture porosity, pore tortuosity and pore-throat radius, respectively (Nooruddin and Hossain, 2012). The resultant permeability equation can be written as (detailed derivation is referred to Li et al. (2016)):

$$k = 0.07(0.078D_p - 0.605D_p p_{closure}^{2/3} T_1^{2/3})^2$$
$$\times \left\{ 1 - \frac{\frac{\pi}{3}ND_p^3 - \frac{\pi}{4}D_p^3 p_{closure}^{4/3} T_3 + \frac{\pi}{4}D_p^3 p_{closure}^2 T_4}{\{w_p^o - 1.89D_p p_{closure}^{2/3}[(n_1 - 1)T_1^{2/3} + T_2^{2/3}]\} \times 10^2} \right\} \tag{34}$$

where

$$\begin{cases} N = ceil\left(0.986\frac{w_p^o}{D_p}\right)n_2 \\ T_3 = 6.5(N - n_2)T_1^{4/3} + 7.15n_2 T_2^{4/3} \\ T_4 = 2.25(N - n_2)T_1^{4/3} + 4.5n_2 T_2^{4/3} \\ n_2 = \frac{2}{\sqrt{3}D_p^2} \times 10^2 \end{cases} \tag{35}$$

In Eq. (35), N represents the number of proppant. Then, the conductivity of propped fracture can be obtained by combing Eqs. (32) and (34), that is $C_f = kw_p$. It should be noted that for the closed portion of the fracture where no proppant exists (as shown in Fig. 3), the fracture permeability is assumed to be zero as it is much smaller compared to the propped portion. Finally, the average conductivity of a fracture can be written as

$$C_F = \frac{\int_0^{s_{tip}} C_f(s)ds}{l} \tag{36}$$

where l represents the length of the fracture.

The crushing of proppant plays a critical role in conductivity
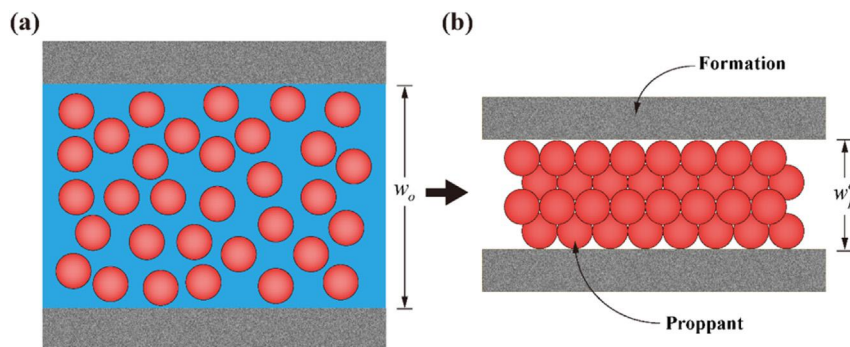

Fig. 2. (a) Illustration of proppant inside a fracture at the end of the pumping and before the fracture is propped. (b) Illustration of multilayer-packed proppant after the fracture is propped and under no closure stress.
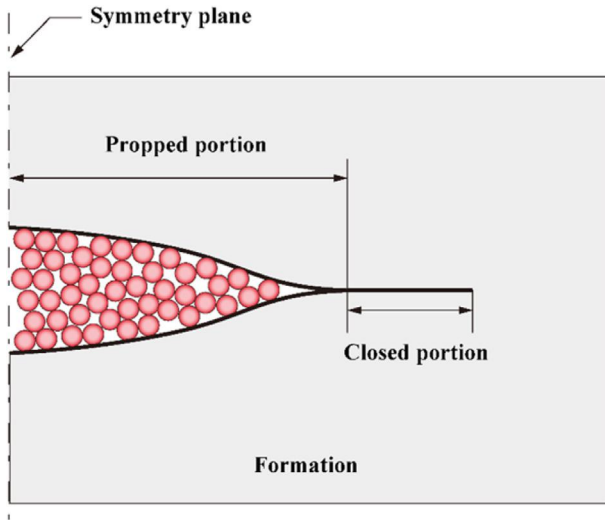
Fig. 3. Illustration of the propped portion with proppant and the closed portion without proppant of a fracture in a symmetry model.

damage (Wang, 2016; Seales et al., 2017) and it must be considered in the numerical model. Due to the fact that the proppant grains are usually treated as a brittle material and the failure is a sudden process rather than a gradual plastic deformation process (Zhang et al., 1990; Ouwerkerk, 1991), plastic deformation has not been considered in this study. It is assumed that the grains failure starts when the maximum tensile stress reaches the tensile strength of the grain (Johnson et al., 1973). For the contact between two proppant grains under the action of force F ($F = D_p^2 p_{closure} \sqrt{3}/2$(Li et al., 2016)), the stress components are all compressive except the radial stress at the edge and outside the contact circle. The distribution of the radial stress near the contact circle can be written as (Johnson, 1985):

$$\sigma_r = p_m \left\{ \frac{1 - 2\nu_p}{3} \left(\frac{a^2}{r^2} \right) \left[1 - \left(1 - \frac{r^2}{a^2} \right)^{3/2} \right] - \left(1 - \frac{r^2}{a^2} \right)^{1/2} \right\}, \quad r \leq a$$

(37a)

$$\sigma_r = p_m \frac{1 - 2\nu_p}{3} \left(\frac{a^2}{r^2} \right), \quad r > a$$

(37b)

where a is the radius of the contact circle and

$$a = \left[\frac{3}{8} F D_p \left(\frac{1 - \nu_p^2}{E_p} \right) \right]^{1/3}$$

(38)

p_m is the maximum contact pressure at the center of the contact and

$$p_m = \frac{3F}{2\pi a^2}$$

(39)

Then, the maximum value of the radial stress, which is also the maximum tensile stress, can be written as

$$\sigma_t = \sigma_r |_{r=a} = \frac{p_m (1 - 2\nu_p)}{3}$$

(40)

Finally, after combing Eqs. (38)–(40) we can obtain

$$\sigma_t = \frac{(\sqrt{3} p_{closure}/2)^{1/3} (1 - 2\nu_p)}{2\pi \left[\frac{3}{8} \left(\frac{1 - \nu_p^2}{E_p} \right) \right]^{2/3}}$$

(41)

Once the proppant starts to fail, it still remains a big challenge to mathematically describe the geometric changes and resulting changes of fracture width and conductivity due to the extreme complexity of this problem. The damage theory has been widely used to describe the failure of granular materials (Gambarotta and Lagomarsino, 1993;

Sokolinsky et al., 2011). Therefore, a damage model is proposed in this study:

$$\omega = \begin{cases} 0, & 0 < \sigma_t < \sigma_t^f \\ \frac{\sigma_t^u (\sigma_t - \sigma_t^f)}{\sigma_t (\sigma_t^u - \sigma_t^f)}, & \sigma_t^f \leq \sigma_t < \sigma_t^u \end{cases}$$

(42)

where ω is damage factor ($0 \leq \omega \leq 1$), σ_t^f is the tensile stress when the grains start to fail, σ_t^u is tensile stress when the grains are totally cracked and is taken as 1000 MPa in this study. Then, the permeability k can be replaced by $k_D = (1 - \omega)k$ (Seales et al., 2017).

It is well known that the conductivity of larger proppants falls below the conductivity of smaller proppants with increasing closure stress. In other words, there is significant size effect on the strength of proppant grains (Huang et al., 2014). However, if we consider the case of a homogeneous spheroidal grain under the action of diametral compression, as given in Eq. (41), it can be clearly seen that the bearing capacity is independent of the grain size. Obviously, this conclusion is not in accordance with the practical experience. In this paper, using the Griffith and Weibull theories, we proposed a theoretical approach allowing to consider the size effect on the strength of proppant grains. According to the Griffith theory (Griffith, 1921), the failure phenomena of grains can be explained by the presence and propagation of microcracks, i.e., the Griffith cracks. The Griffith cracks are randomly distributed with a certain density and the number of Griffith cracks increases with the grain volume. In addition, Weibull (1939) found a relationship between the strength of a specimen and its volume:

$$\sigma_t^f = \sigma_t^o \left(\frac{V}{V_o} \right)^{-1/m}$$

(43)

where σ_t^o is the strength of a specimen of unit volume V_o; m is the Weibull's modulus and is taken as 11 in this paper (Tsoungui et al., 1999), and if $m \to \infty$, then the grain tends to be a perfect homogeneous material and its strength is independent of its volume.

2.7. Iteration scheme to determine the width of propped fracture

After the pumping is finished, the fluid pressure will gradually drop and finally vanish. Thus, the original equilibrium equation (Eq. (20)) can be rewritten as

$$\mathbf{K}\mathbf{U} - \mathbf{F}^{ext} = 0$$

(44)

Since $\mathbf{K}$ is relevant to the unknown $\mathbf{U}$, the above equation is nonlinear and should also be solved iteratively. Similarly, the Newton-Raphson iteration method is adopted to solve the nonlinear problem. The residual vector $\mathbf{R}^i$ of the Newton-Raphson method at the iteration step i can be written as

$$\mathbf{R}^i = \mathbf{K}^i \mathbf{U}^i - \mathbf{F}^{ext}$$

(45)

and the associated Jacobian matrix reads

$$\mathbf{J} = \mathbf{K}^i$$

(46)

Therefore, $\mathbf{U}$ can be updated at each iteration step by

$$\mathbf{U}^{i+1} = \mathbf{U}^i - \frac{\mathbf{R}^i}{\mathbf{J}^i}$$

(47)

The iteration converges when the residual vector $\mathbf{R}^i$ is small enough in comparison with the initial residual vector $\mathbf{R}^0$

$$\eta_{propped} = \|\mathbf{R}^i\| / \|\mathbf{R}^0\| \leq \varepsilon_{tol}^{propped}$$

(48)

where the tolerance $\varepsilon_{tol}^{propped}$ is taken as 10^{-10} in this study.

The normal distance between two fracture surfaces is determined according to the constitutive relation between $P_{closure}$ and w_p. Meanwhile, the relative movement between the two surfaces in the tangential direction is always free. Thus, the matrix $\mathbf{D}^{propped}$ in Eq. (22) can be written as

$$\mathbf{D}^{propped} = \frac{\partial p_{closure}}{\partial w_p}\big(\mathbf{n}_{\Gamma PF} \otimes \mathbf{n}_{\Gamma PF}\big) \tag{49}$$

and evaluated by numerical differentiation. Because Eq. (32) is a transcendental equation without analytical solution, the Secant iteration method (Press et al., 1992) is utilized to calculate $P_{closure}$ for a given w_p.

It should be remarked that for the closed portion of the fracture where no proppant exists, as shown in Fig. 3, the contact status between frictional fracture surfaces under the action closure stress needs to be determined. This can be easily achieved by replacing $\mathbf{D}^{propped}$ with $\mathbf{D}^{contact}$, which is expressed as follows within the framework of plasticity theory of friction (Khoei et al., 2015; Khoei and Nikbakht, 2007):

$$\mathbf{D}^{contact} = \begin{cases} k_N(\mathbf{n}_{\Gamma PF} \otimes \mathbf{n}_{\Gamma PF}) + k_T(\mathbf{I} - \mathbf{n}_{\Gamma PF} \otimes \mathbf{n}_{\Gamma PF}) & \text{for stick} \\ k_N(\mathbf{n}_{\Gamma PF} \otimes \mathbf{n}_{\Gamma PF}) + \mu_f k_T(\mathbf{I} - \mathbf{n}_{\Gamma PF} \otimes \mathbf{n}_{\Gamma PF}) & \text{for slip} \end{cases} \tag{50}$$

where k_N and k_T are the penalty parameters in the normal and tangential directions, respectively; μ_f is the Coulomb friction coefficient, and $\mathbf{I}$ is the identity tensor. In this study, k_N, k_T are both taken as 10^4 GPa/m and μ_f is taken as 0.2.

3. Verification

Verification of the fluid-solid coupling model against analytical solutions and proppant transport in a single fracture have been performed in our previous study (Shi et al., 2016). In order to verify the proposed XFEM-based numerical method for determining the conductivity of propped fracture under the influence of closure stress, four verification examples are presented and compared with the experimental results (Wen et al., 2007; Seales et al., 2017). Parameters of the four cases are listed in Table 1. The plane strain model of these verification examples is illustrated in Fig. 4. The model is meshed into 400 four-node quadrilateral elements of size 0.5 m × 0.5 m.

The simulation results and comparisons with experimental data are presented in Figs. 5–7. It can be found that the proposed model is able to predict satisfactory fracture conductivities which are nonlinearly related to the applied closure stresses. It should be noted that in Fig. 5 the simulated conductivities are somewhat less than the experimental results. One possible reason is that the mechanical interaction (Hopkins, 2000; Kamali and Pournik, 2016) has not been taken into account in the proposed model. It can also be concluded from Figs. 6 and 7 that proppant crushing plays a critical role in conductivity damage. In other words, the calculated conductivity is much higher than the experimental data if proppant crushing has not been properly considered. In addition, from the perspective of numerical computation, it is found that 7 to 11 Newton-Raphson iterations are required to reach convergence for a given closure stress, and 4 to 6 Secant iterations are performed in each Newton-Raphson iteration.

4. Results and discussion

Based on the numerical model presented above, we set up and analyze a base case and then conduct the sensitivity studies to investigate the influence of several factors on fracture conductivity. All simulations share the same symmetrical model as shown in Fig. 8. The
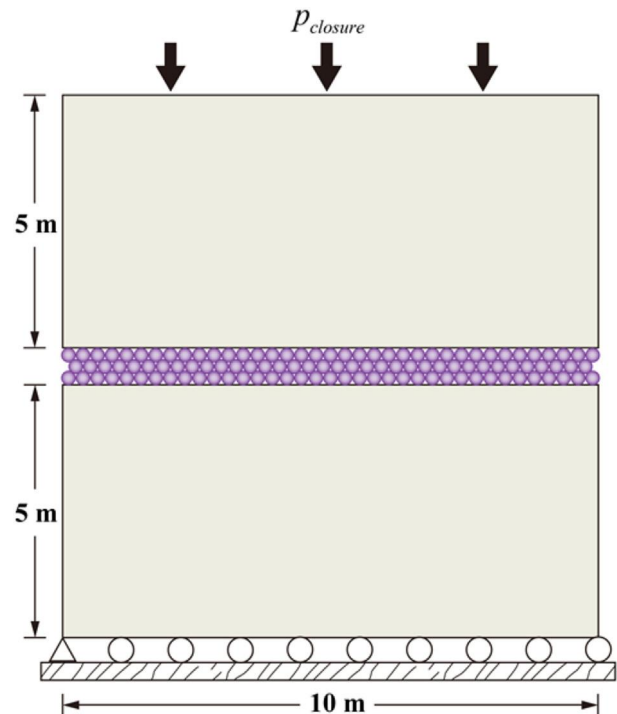

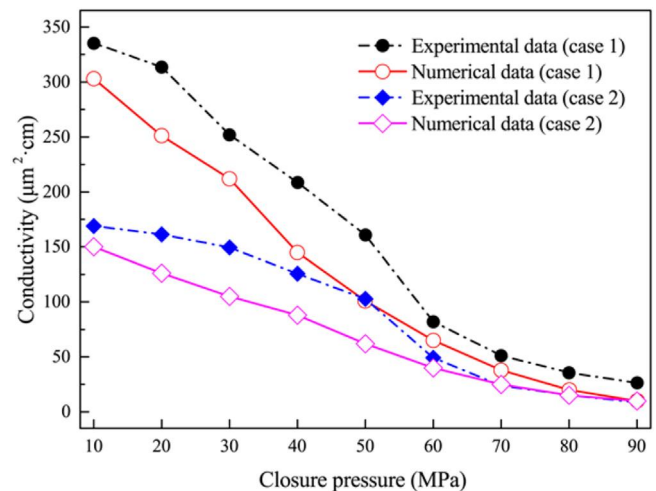**Fig. 4.** Schematic diagram of a propped fracture of constant width inside the formation.

Fig. 5. Comparisons of the numerical values of fracture conductivity and experimental data under different closure pressures for case 1 and case 2.

left edge of the model is fixed in x direction and the bottom-left corner is fixed in both x and y directions. The initial hydro-fracture is positioned on the left edge of the model. The model is meshed into 2220 four-node quadrilateral elements and the size of elements around the

Table 1
Properties of formation and proppant of the verification examples.

| Parameter	Unit	Case 1 (Wen et al., 2007)	Case 2 (Wen et al., 2007)	Case 3 (Seales et al., 2017)	Case 4 (Seales et al., 2017)
Elastic modulus of formation E	GPa	12.76	12.76	20	20
Poisson's ratio of formation ν	−	0.32	0.32	0.25	0.25
Elastic modulus of proppant E_p	GPa	60	60	80	110
Poisson's ratio of proppant ν_p	−	0.17	0.17	0.2	0.2
Average proppant size D_p	mm	0.63	0.42	0.315	0.315
Strength of proppant $\sigma o\, t$	MPa	80	80	60	65
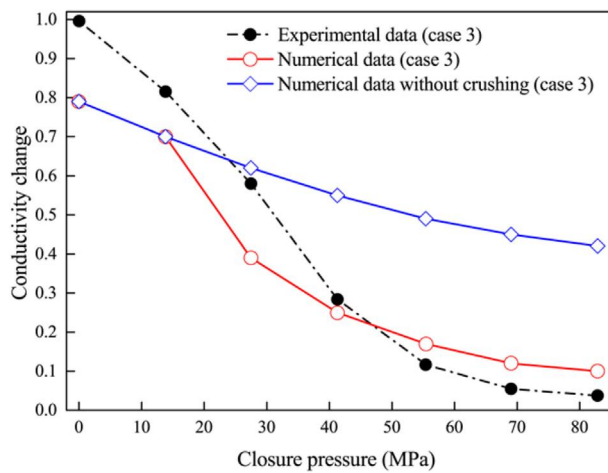
Fig. 6. Comparisons of the numerical values (with and without crushing) of normalized fracture conductivity and experimental data under different closure pressures for case 3.
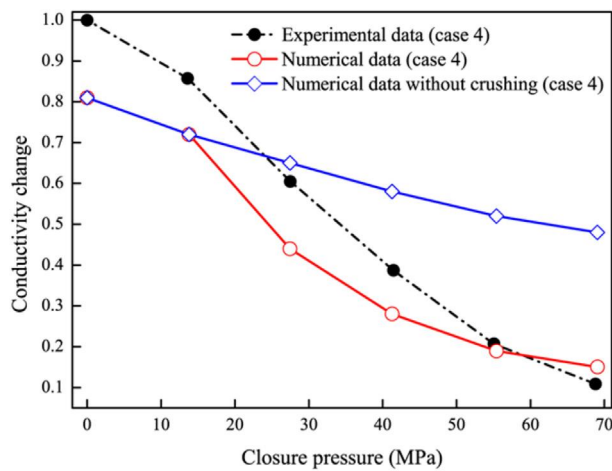

Fig. 7. Comparisons of the numerical values (with and without crushing) of normalized fracture conductivity and experimental data under different closure pressures for case 4.

Fig. 8. Geometry and finite element mesh of symmetrical hydraulic fracture propagation model.

Table 2

Material properties, fracturing parameters and in-situ stresses of the base case.

Parameter	Unit	Value
Elastic modulus of formation E	GPa	20.0
Poisson's ratio of formation ν	−	0.2
Fracture toughness of formation K_{IC}	MPa·m$^{1/2}$	1.0
Elastic modulus of proppant E_p	GPa	20.0
Poisson's ratio of proppant ν_p	−	0.2
Proppant size D_p	mm	0.6
Pumping rate of slurry Q_{inj}	m^2/s	0.001
Pumping concentration of proppant c_{inj}	−	0.3
Fluid viscosity μ	Pa·s	0.1
In-situ stress in x direction σ_H	MPa	100
In-situ stress in y direction σ_h	MPa	30
Strength of proppant $\sigma o\ t$	MPa	50

hydro-fracture (colored in pink) is 0.5 m × 0.5 m.

For the base case, material properties, fracturing parameters and in-situ stresses are listed in Table 2. The fracture propagation regime is viscosity-dominated as K_m equals 0.313 (Hu and Garagash, 2010). For all simulations, the proppant is injected at a constant concentration after pumping time reaches 20 s in addition to the periodic pumping of proppant which will be presented in Section 4.7.

The widely used maximum circumferential tensile stress criterion (Erdogan and Sih, 1963; Shi et al., 2016) is utilized to predict the propagation of the hydro-fracture. This criterion assumes that the propagation is along the direction normal to the maximum hoop tensile stress. Besides, when the equivalent stress intensity factor K_e is greater than or equal to the fracture toughness of the rock formation, the fracture will propagate. The domain forms of the interaction integral method (Moran and Shih, 1987) are employed to determine the stress intensity factors K_I and K_{II}. The equivalent stress intensity factor K_e can be written as

$$K_e = \cos\frac{\theta}{2}\left(K_I \cos^2\frac{\theta}{2} - \frac{3K_{II}}{2}\sin\theta\right) \tag{51}$$

where θ is the fracture propagation angle in the local fracture tip coordinate system and can be determined (Stone and Babuška, 1998) by
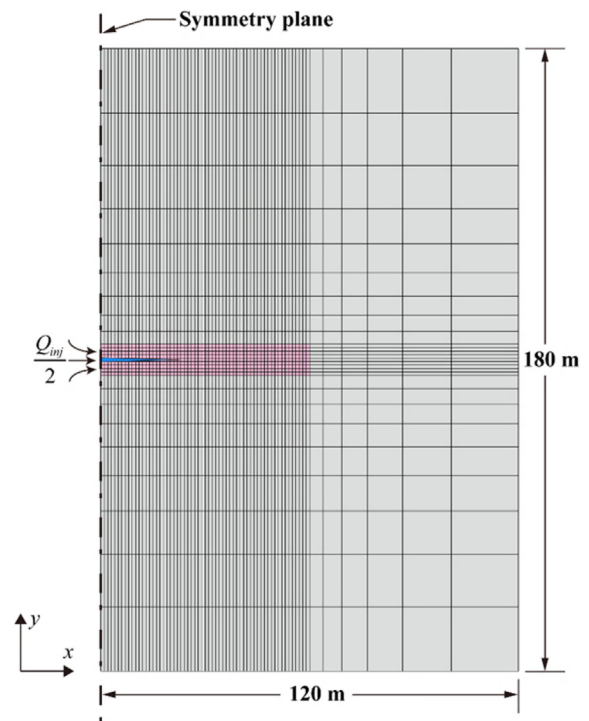
$$\theta = 2\arctan\left(\frac{-2K_{II}/K_I}{1 + \sqrt{1 + 8(K_{II}/K_I)^2}}\right) \tag{52}$$

The initial half-length of the hydro-fracture is 1.5 m. A uniform pressure of 3.6 MPa, which is the theoretical fluid pressure (Hu and Garagash, 2010) at the pumping point, is taken as the initial guess for the first time step of the Newton-Raphson iteration. For the subsequent time steps, the pressure solution obtained from the previous time step is chosen as the initial estimate. Simulations continue until the fracture length reaches 50.5 m.

The uncertainty parameters of the sensitivity studies include proppant size, elastic modulus of proppant, elastic modulus of formation, Poisson's ratio of proppant, Poisson's ratio of formation, pumping rate of slurry, proppant concentration, and pumping strategy of proppant. As the selected ranges of uncertainty parameters are critical to a sensitivity analysis, wide ranges covering a large variety of scenarios possibly encountered in practice are considered in this study and are listed in Table 3.

Table 3
Uncertainty parameters used in sensitivity studies.

Parameter	Base case	Minimum	Maximum	Increment	Unit
Proppant size D_p	0.6	0.1	2.0	0.1	mm
Elastic modulus of proppant E_p	20	5	80	5	GPa
Elastic modulus of formation E	20	5	80	5	GPa
Poisson's ratio of proppant ν_p	0.2	0.1	0.3	0.05	−
Poisson's ratio of formation ν	0.2	0.1	0.3	0.05	−
Pumping rate of slurry Q_{inj}	0.001	0.0005	0.005	0.0005	m²/s
Pumping concentration of proppant c_{inj}	0.3	0.05	0.5	0.05	−

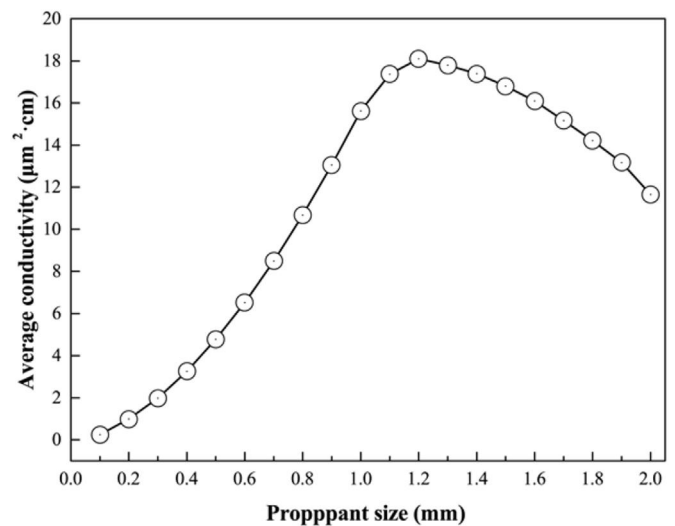**Fig. 10.** Effect of proppant size on the average conductivity of propped fracture.
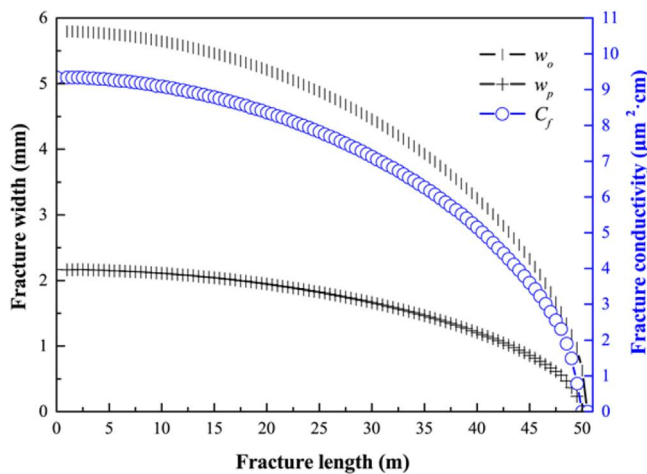
Fig. 9. Simulation results of the base case including fracture width after the pumping is finished w_o, width of the propped fracture under in-situ stress w_p, and fracture conductivity C_f.

Fig. 11. Effects of elastic moduli of proppant and formation on the average conductivity of propped fracture.

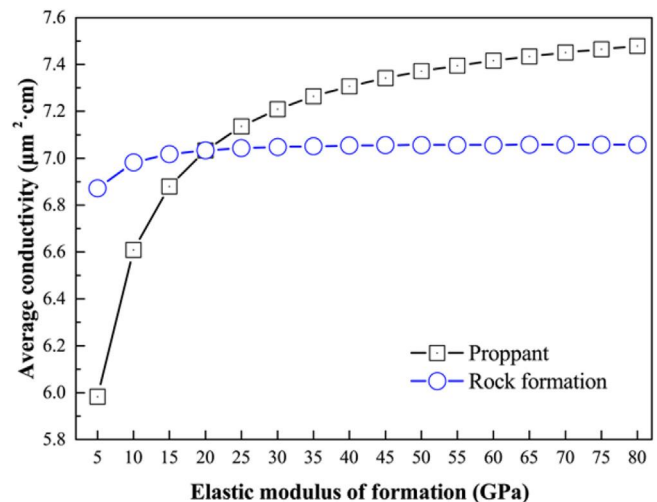### 4.1. Results of the base case

Simulation results of the base case are presented in Fig. 9. Specifically, the fracture width at the pumping point after the pumping is finished is 5.8 mm. Then, after the hydraulic pressure is relieved and under the action of closure stress, the final width of the propped fracture at the pumping point drops to 2.2 mm. In addition, the conductivity at the pumping point and the average conductivity of the propped fracture are 9.31 μm² cm and 7.05 μm² cm, respectively.

4.2. Effect of proppant size

The optimization of proppant size is very important to achieve the desired well productivity. Proppant grains with average diameters ranging from 0.1 mm to 2.0 mm have been studied. Results are shown in Fig. 10. It can be seen that the conductivity increases and then decreases as D_p increases. In general, it is known that larger proppant grains result in larger fracture conductivity (Cooke, 1975; Lacy et al., 1997; Fredd et al., 2001). This is because the permeability of the propped fracture is proportional to the square of the pore-throat radius which is directly related to the proppant size (see Li et al., 2016 for more details). However, this positive trend of conductivity induced by increasing proppant size is counteracted by the negative trend induced by the following two major factors: (1) the size effect on the strength of proppant grains, i.e., the tensile strength decreases as grain size increases; and (2) large proppant is difficult to be transported to the near-tip region of the fracture. Under the combined effect of these three factors, the average conductivity is presented as a single-peak curve

with the peak appearing at 1.21 mm, as shown in Fig. 10.

4.3. Effects of elastic moduli of proppant and formation

Fig. 11 presents the effects of elastic modulus of proppant E_p ranging from 5 GPa to 80 GPa. It can be observed that the fracture conductivity increases significantly when E_p is relatively small and then tends to be a constant value as E_p continues to increase. From the perspective of mathematical model, the reason for the decreasing impact of elastic modulus on the conductivity at higher elastic modulus values is the complex non-linear relationship between the conductivity and the elastic modulus, which can be seen from Eq. (32) and Eq. (34). Simply speaking, the conductivity is not proportional to the elastic modulus. In addition, the conductivity of the propped fracture is still a finite value even the proppant has an infinite value of elastic modulus (i.e., treat the proppant grain as a rigid body). Therefore, the conductivity of the propped fracture should approach a constant value with increasing elastic modulus of proppant.

The range of fracture conductivity is 5.9 μm² cm to 7.47 μm² cm. The effect of elastic modulus of formation E on fracture conductivity is also shown. A similar conclusion can be drawn. However, the range of fracture conductivity, which is 6.9 μm² cm to 7.06 μm² cm, is much
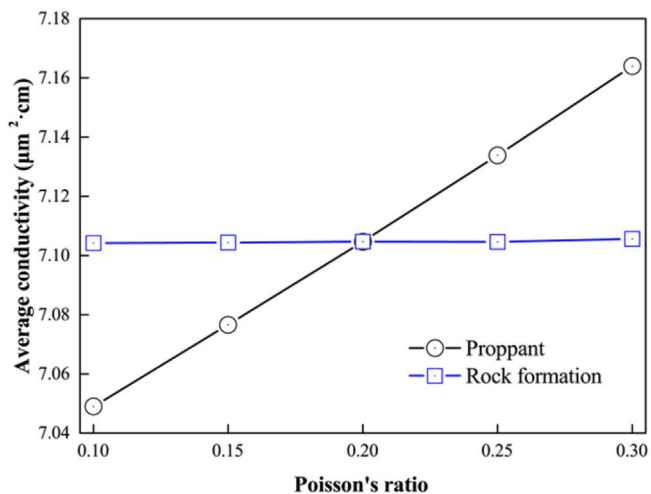
Fig. 12. Effects of Poisson's ratios of proppant and formation on the average conductivity of propped fracture.
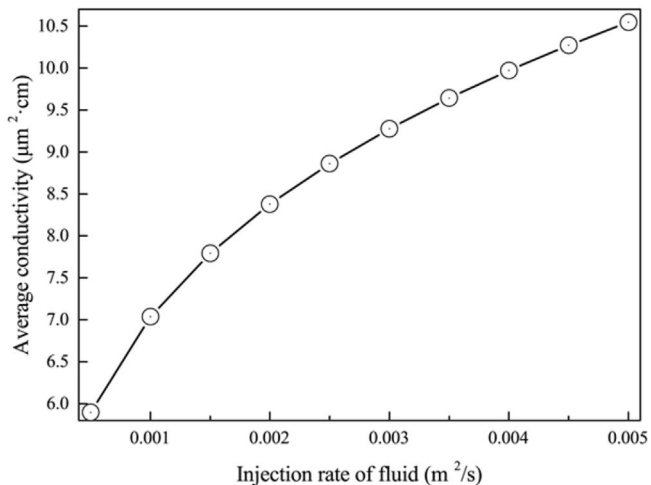

Fig. 13. Effect of pumping rate of slurry on the average conductivity of propped fracture.
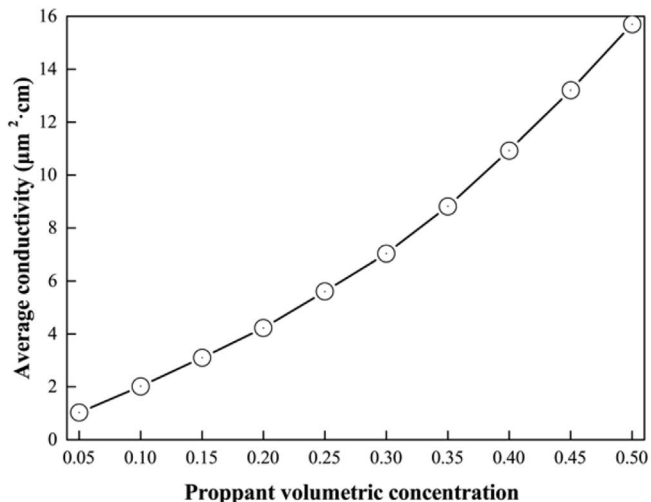

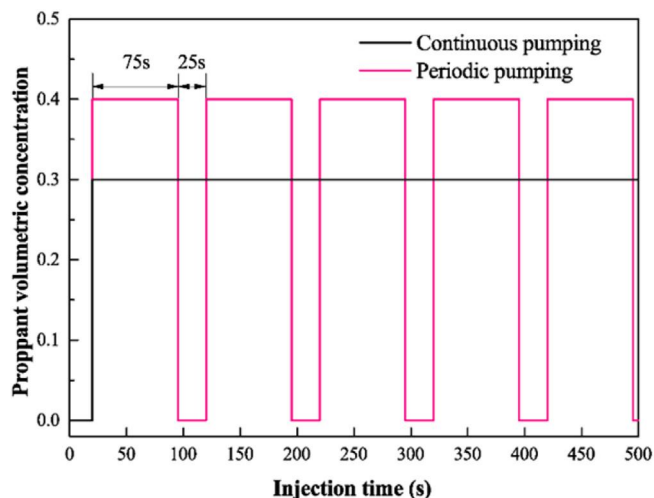**Fig. 14.** Effect of proppant concentration on the average conductivity of propped fracture.

Fig. 15. Curves of time-dependent proppant volumetric concentration at the pumping point of continuous pumping and periodic pumping.
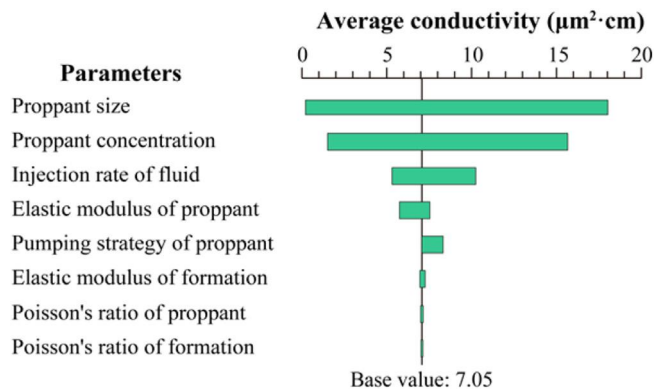

Fig. 16. Tornado diagram of sensitivity studies.

narrower than that obtained by changing E_p, indicating that E_p is much more critical than E in the calculation of fracture conductivity.

4.4. Effects of Poisson's ratios of proppant and formation

When calculating the deformation of particles along the normal direction of the fracture surface, the Poisson's ratios of proppant and formation are required parameters and must be considered in the mathematical model when using the Hertzian contact theory. Therefore, it is of significance to study the effect of Poisson's ratios according to the proposed mathematical model.

Fig. 12 presents the effects of Poisson's ratios of proppant (ν_p) and formation (ν) ranging from 0.1 to 0.3. It can be observed that the fracture conductivity increases linearly with increasing ν_p. However, fracture conductivity keeps unchanged with increasing ν, indicating that the Poisson's ratio of formation has no effect on fracture conductivity according to the proposed mathematical model.

4.5. Effect of pumping rate of slurry

Fig. 13 shows the effect of pumping rate of slurry Q_{inj} on fracture conductivity. The range of investigated Q_{inj} is 0.0005 m^2/s to 0.005 m^2/s. It can be seen that the average conductivity increases as Q_{inj} increases but the increasing rate slows down gradually. It should be noted that although larger pumping rate of slurry leads to larger fracture conductivity, sometimes, the pumping rate is limited by some other factors, such as wellbore profile, perforation area and fracturing equipment (Economides and Martin, 2007).

4.6. Effect of proppant volumetric concentration

The effect of the proppant volumetric concentration at the pumping point (c_{inj}) on fracture conductivity is illustrated in Fig. 14. It can be found that the average conductivity increases with increasing c_{inj} in a nonlinear manner. This is an obvious consequence as more proppant is able to be injected into the fracture when c_{inj} increases. The simulation results are in accordance with the widely accepted conclusion which says that higher proppant concentrations within a proppant pack are proportional to increased fracture width and therefore relatively proportional to increasing fracture conductivity (Economides and Martin, 2007).

4.7. Effect of pumping strategy of proppant

Recently, some heterogeneous proppant placement techniques such as the channel fracturing technique, where the proppant is intermittently pumped, have been developed and practiced (Barasia and Pankaj, 2014). In the base case, the proppant is injected at a constant volumetric concentration of 0.3. In the case of this section, the proppant is periodically injected at a higher volumetric concentration of 0.4. For both pumping strategies, the amounts of proppant are kept the same. For the periodic pumping, the proppant is injected for 75 s within a period of 100 s, as shown in Fig. 15. Simulation results show that the average conductivity increases by 21% from 7.05 μm² cm to 8.51 μm² cm compared to the base case. It is demonstrated that the fracture conductivity may be improved by applying periodic pumping of proppant.

Finally, the impacts of the above uncertainty parameters on the final fracture conductivity are summarized in a Tornado diagram shown in Fig. 16 based on the ranges investigated. It is shown that the most sensitive parameter is proppant size, followed by volumetric concentration of proppant, pumping rate of the slurry, and elastic modulus of proppant. The pumping strategy of proppant is less sensitive. The elastic modulus of formation and Poisson's ratio of proppant are negligible compared to other factors. The Poisson's ratio of formation has no effect on fracture conductivity.

5. Conclusions

We presented a coupled numerical model to calculate the conductivity of propped fracture considering proppant transport, placement, deformation, embedment, and crushing in the context of the extended finite element method. We calculated the average conductivity of propped fracture according to fracture width which is related to the closure stress by a nonlinear constitutive relation. We took into account the proppant crushing process by introducing a damage model. We considered the size effect of proppant grains on the crushing strength using the Griffith and Weibull theories. Then, we performed sensitivity studies on some parameters varied over wide ranges based on the proposed model. The following conclusions can be drawn from this study:

(1) The verification examples and comparisons with experimental data indicate that proppant crushing plays a critical role in conductivity damage and must be properly considered in the numerical model.
(2) The sensitivity study shows that the most sensitive factor is the proppant size and fracture conductivity increases firstly and then decreases with increasing proppant size. There are two main reasons for this: first, the tensile strength decreases as grain size increases, i.e., the size effect on the strength of proppant grains; second, the large proppant is not able to pass the narrow portion of the hydro-fracture, such as the near-tip region.
(3) In addition to proppant size, the most sensitive factor is proppant concentration, followed by pumping rate of slurry, elastic modulus of proppant, and pumping strategy of proppant. Furthermore, the

effects of elastic modulus of formation and Poisson's ratios of proppant and formation are negligible.
(4) Periodic pumping of proppant leads to higher conductivity than continuous pumping while keeping the amount of injected proppant constant.

By systematically considering a series of complex physical processes and a variety of factors, and benefiting from the advantages of the extended finite element method, the proposed numerical model is able to satisfactorily and effectively predict the conductivity of propped fracture. The proposed model is a useful tool for proppant selection for given formation conditions in hydraulic fracturing design.

References

Adachi, J., Siebrits, E., Peirce, A., Desroches, J., 2007. Computer simulation of hydraulic fractures. Int. J. Rock. Mech. Min. Sci. 44 (5), 739–757.
Alramahi, B., Sundberg, M.I., 2012. Proppant embedment and conductivity of hydraulic fractures in shales. In: 46th U.S. Rock Mechanics/Geomechanics Symposium. American Rock Mechanics Association, Chicago, Illinois, USA.
Awoleke, O.O., Romero, J.D., Zhu, D., Hill, D., 2012. Experimental investigation of propped fracture conductivity in tight gas reservoirs using factorial design. In: SPE Hydraulic Fracturing Technology Conference. Society of Petroleum Engineers, The Woodlands, Texas, USA.
Barasia, A., Pankaj, P., 2014. Tail-in Proppant and its Importance in Channel Fracturing Technique, SPE Bergen One Day Seminar. Society of Petroleum Engineers, Bergen, Norway.
Batchelor, G.K., 1967. An Introduction to Fluid Dynamics. Cambridge University Press, Cambridge.
Belytschko, T., Black, T., 1999. Elastic crack growth in finite elements with minimal re-meshing. Int. J. Numer. Methods Eng. 45, 601–620.
Cooke, C.E., 1975. Effect of fracturing fluids on fracture conductivity. J. Petrol. Technol. 27 (10), 1273–1282.
Crouch, S.L., Starfield, A.M., 1983. Boundary Element Methods in Solid Mechanics: with Applications in Rock Mechanics and Geological Engineering. George Allen & Unwin, London.
Dahi-Taleghani, A., Olson, J.E., 2011. Numerical modeling of multistranded-hydraulic-fracture propagation: accounting for the interaction between induced and natural fractures. SPE J. 16 (3), 575–581.
Dontsov, E.V., Peirce, A.P., 2015. Proppant transport in hydraulic fracturing: crack tip screen-out in KGD and P3D models. Int. J. Solids Struct. 63, 206–218.
Economides, M.J., Martin, T., 2007. Modern Fracturing Enhancing Natural Gas Production. BJ Services Company, Houston, TX.
Erdogan, F., Sih, G.C., 1963. On the crack extension in plates under plane loading and transverse shear. J. Basic. Eng-T. ASME. 85 (4), 519–525.
Fredd, C.N., McConnell, S.B., Boney, C.L., England, K.W., 2001. Experimental study of fracture conductivity for water-fracturing and conventional fracturing applications. SPE J. 6 (3), 288–298.
Gambarotta, L., Lagomarsino, S., 1993. A microcrack damage model for brittle materials. Int. J. Solids. Struct. 30, 177–198.
Gao, Y., Lv, Y., Wang, M., Li, K., 2012. New Mathematical Models for Calculating the Proppant Embedment and Fracture Conductivity, SPE Annual Technical Conference and Exhibition. Society of Petroleum Engineers, San Antonio, Texas, USA.
Gordeliy, E., Peirce, A., 2013a. Coupling schemes for modeling hydraulic fracture propagation using the XFEM. Comput. Method. Appl. M. 253, 305–322.
Gordeliy, E., Peirce, A., 2013b. Implicit level set schemes for modeling hydraulic fractures using the XFEM. Comput. Method. Appl. M. 266, 125–143.
Griffith, A.A., 1921. The phenomena of rupture and flow in solids. Philos. Trans. R. Soc. Lond. 221, 163–198.
Hammond, P.S., 1995. Settling and slumping in a Newtonian slurry, and implications for proppant placement during hydraulic fracturing of gas wells. Chem. Eng. Sci. 50 (20), 3247–3260.
Han, J., Wang, J.Y., Puri, V., 2016a. A fully coupled geomechanics and fluid flow model for proppant pack failure and fracture conductivity damage analysis. J. Nat. Gas. Sci. Eng. 31, 546–554.
Han, J., et al., 2016b. Numerical study of proppant transport in complex fracture geometry. In: SPE Low Perm Symposium. Society of Petroleum Engineers, Denver, Colorado, USA.
Hirsch, C., 1990. Numerical Computation of Internal and External Flows Volume 2: Computational Methods for Inviscid and Viscous Flows. John Wiley & Sons, New York.
Hopkins, D.L., 2000. The implications of joint deformation in analyzing the properties

and behavior of fractured rock masses, underground excavations, and faults. Int. J. Rock. Mech. Min. 37, 175–202.

Huang, J., Xu, S., Yi, H., Hu, S., 2014. Size effect on the compression breakage strengths of glass particles. Powder Technol. 268, 86–94.

Hu, J., Garagash, D.I., 2010. Plane-strain propagation of a fluid-driven crack in a permeable rock with fracture toughness. J. Eng. Mech. 136 (9), 1152–1166.

Johnson, K.L., O'Connor, J.J., Woodward, A.C., 1973. The effect of the indenter elasticity on the Hertzian fracture of brittle materials. Proc. Roy. Soc. Lond. A334, 95–117.

Johnson, K.L., 1985. Contact Mechanics. Cambridge University Press, Cambridge.

Kamali, A., Pournik, M., 2016. Fracture closure and conductivity decline modeling – application in unpropped and acid etched fractures. J. Unconv. Oil Gas Resour. 14, 44–55.

Khoei, A.R., Hirmand, M., Vahab, M., Bazargan, M., 2015. An enriched FEM technique for modeling hydraulically driven cohesive fracture propagation in impermeable media with frictional natural faults: numerical and experimental investigations. Int. J. Numer. Methods Eng. 104 (6), 439–468.

Khoei, A.R., Nikbakht, M., 2007. An enriched finite element algorithm for numerical computation of contact friction problems. Int. J. Mech. Sci. 49 (2), 183–199.

Khoei, A.R., Vahab, M., Hirmand, M., 2016. Modeling the interaction between fluid-driven fracture and natural fault using an enriched-FEM technique. Int. J. Fract. 197, 1–24.

Kong, B., Fathi, E., Ameri, S., 2015. Coupled 3-D numerical simulation of proppant distribution and hydraulic fracturing performance optimization in Marcellus shale reservoirs. Int. J. Coal Geol. 147–148, 35–45.

Lacy, L.L., Rickards, A.R., Ali, S.A., 1997. Embedment and Fracture Conductivity in Soft Formations Associated with HEC, Borate and Water-based Fracture Designs, SPE Annual Technical Conference and Exhibition. Society of Petroleum Engineers, San Antonio, Texas, USA.

Lacy, L.L., Rickards, A.R., Bilden, D.M., 1998. Fracture width and embedment testing in soft reservoir sandstone. SPE Drill. Complet. 13 (1), 25–29.

Lecampion, B., 2009. An extended finite element method for hydraulic fracture problems. Commun. Numer. Methods Eng. 25 (2), 121–133.

Li, H., Wang, K., Xie, J., Li, Y., Zhu, S., 2016. A new mathematical model to calculate sand-packed fracture conductivity. J. Nat. Gas. Sci. Eng. 35, 567–582.

Li, K., Gao, Y., Lyu, Y., Wang, M., 2015. New mathematical models for calculating proppant embedment and fracture conductivity. SPE J. 20 (3), 496–507.

Lopez-Hernandez, H.D., Valko, P.P., Pham, T.T., 2004. Optimum fracture treatment design minimizes the impact of non-Darcy flow effects. In: SPE Annual Technical Conference and Exhibition. Society of Petroleum Engineers, Houston, Texas, USA.

Moës, N., Dolbow, J., Belytschko, T., 1999. A finite element method for crack growth without remeshing. Int. J. Numer. Methods Eng. 46 (1), 131–150.

Mohammadnejad, T., Khoei, A.R., 2013a. An extended finite element method for hydraulic fracture propagation in deformable porous media with the cohesive crack model. Finite Elem. Anal. Des. 73, 77–95.

Mohammadnejad, T., Khoei, A.R., 2013b. Hydro-mechanical modeling of cohesive crack propagation in multiphase porous media using the extended finite element method. Int. J. Numer. Anal. Methods Geomech. 37 (10), 1247–1279.

Moran, B., Shih, C.F., 1987. Crack tip and associated domain integrals from momentum and energy balance. Eng. Fract. Mech. 27 (6), 615–642.

Neto, L.B., Khanna, A., Kotousov, A., 2015. Conductivity and performance of hydraulic fractures partially filled with compressible proppant packs. Int. J. Rock. Mech. Min. Sci. 74, 1–9.

Nooruddin, H.A., Hossain, E., 2012. Modified Kozeny-Carmen correlation for enhanced hydraulic flow unit characterization. J. Pet. Sci. Eng. 80, 107–115.

Ouwerkerk, C.E.D., 1991. A micro-mechanical connection between the single-particle strength and the bulk strength of random packings of spherical particles. Powder Technol. 65, 125–138.

Ouyang, S., Carey, C.F., Yew, C.H., 1997. An adaptive finite element scheme for hydraulic fracturing with proppant transport. Int. J. Numer. Methods Fluids 24 (7), 645–670.

Press, W., Teukolsky, S., Vetterling, W., Flannery, B., 1992. Numerical Recipes in Fortran: the Art of Scientic Computing. Cambridge University Press, New York.

Raymond, S., Aimene, Y., Nairn, J., Ouenes, A., 2015. Coupled fluid-solid geomechanical modeling of multiple hydraulic fractures interacting with natural fractures and the resulting proppant distribution. In: SPE/CSUR Unconventional Resources Conference. Society of Petroleum Engineers, Calgary, Alberta, Canada.

Rivers, M., Zhu, D., Hill, A.D., 2012. Proppant fracture conductivity with high proppant loading and high closure stress. In: SPE Hydraulic Fracturing Technology Conference. Society of Petroleum Engineers, Woodlands, Texas, USA.

Seales, M.B., Dilmore, R., Ertekin, T., Wang, J.Y., 2017. A numerical study of factors affecting fracture-fluid cleanup and produced gas/water in Marcellus shale: Part II. SPE J. 22 (2), 1–19.

Shekhawat, D.S., Pathak, K., 2016. Proppant's performance with reservoir rock under variable closure pressure. J. Pet. Sci. Eng. 147, 34–46.

Shi, F., Wang, X., Liu, C., Liu, H., Wu, H., 2016. A coupled extended finite element approach for modeling hydraulic fracturing in consideration of proppant. J. Nat. Gas. Sci. Eng. 33, 885–897.

Shi, F., Wang, X., Liu, C., Liu, H., Wu, H., 2017. An XFEM-based method with reduction technique for modeling hydraulic fracture propagation in formations containing frictional natural fractures. Eng. Fract. Mech. 173, 64–90.

Shiozawa, S., McClure, M., 2016. Simulation of proppant transport with gravitational settling and fracture closure in a three-dimensional hydraulic fracturing simulator. J. Pet. Sci. Eng. 138, 298–314.

Sokolinsky, V.S., Indermuehle, K.C., Hurtado, J.A., 2011. Numerical simulation of the crushing process of a corrugated composite plate. Compos. Part A 42, 1119–1126.

Steinhaus, H., 1999. Mathematical Snapshots. Dover Publications, New York.

Stone, T.J., Babuška, I., 1998. A numerical method with a posteriori error estimation for determining the path taken by a propagating crack. Comput. Method. Appl. M. 160 (3–4), 245–271.

Sulsky, D., Chen, Z., Schreyer, H.L., 1994. A particle method for history-dependent materials. Comput. Method. Appl. M. 118, 179–196.

Taleghani, A.D., Olson, J.E., 2014. How natural fractures could affect hydraulic-fracture geometry. SPE J. 19 (1), 161–171.

Tomac, I., Gutierrez, M., 2013. Numerical Study of Horizontal Proppant Flow and Transport in a Narrow Hydraulic Fracture. In: 47th U.S. Rock Mechanics/ Geomechanics Symposium. American Rock Mechanics Association, San Francisco, California.

Tong, S., Mohanty, K.K., 2016. Proppant transport study in fractures with intersections. Fuel 181, 463–477.

Tsoungui, O., Vallet, D., Charmet, J.C., Roux, S., 1999. Size effects in single grain fragmentation. Granul. Matter 2, 19–27.

Wang, H., 2016. What factors control shale gas production decline trend: a comprehensive analysis and investigation. In: SPE/IAEE Hydrocarbon Economics and Evaluation Symposium. Society of Petroleum Engineers, Houston, Texas, USA.

Weibull, W., 1939. A statistical theory of the strength of materials. Proc. Roy. Swed. Inst. Eng. 151, 1–45.

Wen, Q., Zhang, S., Wang, L., Liu, Y., Li, X., 2007. The effect of proppant embedment upon the long-term conductivity of fractures. J. Pet. Sci. Eng. 55, 221–227.

Weng, X., Kresse, O., Cohen, C.-E., Wu, R., Gu, H., 2011. Modeling of hydraulic-fracture-network propagation in a naturally fractured formation. SPE Prod. Oper. 26 (4), 368–380.

Yu, W., Zhang, T., Du, S., Sepehrnoori, K., 2015. Numerical study of the effect of uneven proppant distribution between multiple fractures on shale gas well performance. Fuel 142, 189–198.

Zhang, J.X., Wong, T.F., Davis, D.M., 1990. Micromechanics of pressure-induced grain crushing in porous rocks. J. Geophys. Res. 95, 341–352.

Zhang, J., Zhu, D., Hill, D., 2015. A new theoretical method to calculate shale fracture conductivity based on the population balance equation. J. Pet. Sci. Eng. 134, 40–48.

Zhou, L., Houa, M.Z., Goua, Y., Lia, M., 2014. Numerical investigation of a low-efficient hydraulic fracturing operation in a tight gas reservoir in the North German Basin. J. Pet. Sci. Eng. 120, 119–129.

Zoveidavianpoor, M., Gharibi, A., 2015. Application of polymers for coating of proppant in hydraulic fracturing of subterraneous formations: a comprehensive review. J. Nat. Gas. Sci. Eng. 24, 197–209.